Comparison of Methods for Modeling Fractional Cover Using Simulated Satellite Hyperspectral Imager Spectra

Philip E. Dennison [1,*], **Yi Qi** [2], **Susan K. Meerdink** [3], **Raymond F. Kokaly** [4], **David R. Thompson** [5], **Craig S. T. Daughtry** [6], **Miguel Quemada** [7], **Dar A. Roberts** [8], **Paul D. Gader** [3], **Erin B. Wetherley** [8], **Izaya Numata** [9] and **Keely L. Roth** [10]

[1]   Department of Geography, University of Utah, Salt Lake City, UT 84112, USA
[2]   School of Natural Resources, University of Nebraska Lincoln, Lincoln, NE 68583, USA
[3]   Engineering School of Sustainable Infrastructure and Environment, University of Florida, Gainesville, FL 32611, USA
[4]   Geophysics and Geochemistry Science Center, US Geological Survey, Denver, CO 80225, USA
[5]   Jet Propulsion Laboratory, California Institute of Technology, Pasadena, CA 91109, USA
[6]   Hydrology and Remote Sensing Laboratory, US Department of Agriculture Agricultural Research Service, Beltsville, MD 20705, USA
[7]   School of Agricultural Engineering, CEIGRAM, Universidad Politecnica de Madrid, 28040 Madrid, Spain
[8]   Department of Geography, University of California Santa Barbara, Santa Barbara, CA 93106, USA
[9]   Geospatial Sciences Center of Excellence, South Dakota State University, Brookings, SD 57007, USA
[10] Science, The Climate Corporation, San Francisco, CA 94103, USA
*   Correspondence: dennison@geog.utah.edu

check for updates

Abstract: Remotely sensed data can be used to model the fractional cover of green vegetation (GV), non-photosynthetic vegetation (NPV), and soil in natural and agricultural ecosystems. NPV and soil cover are difficult to estimate accurately since absorption by lignin, cellulose, and other organic molecules cannot be resolved by broadband multispectral data. A new generation of satellite hyperspectral imagers will provide contiguous narrowband coverage, enabling new, more accurate, and potentially global fractional cover products. We used six field spectroscopy datasets collected in prior experiments from sites with partial crop, grass, shrub, and low-stature resprouting tree cover to simulate satellite hyperspectral data, including sensor noise and atmospheric correction artifacts. The combined dataset was used to compare hyperspectral index-based and spectroscopic methods for estimating GV, NPV, and soil fractional cover. GV fractional cover was estimated most accurately. NPV and soil fractions were more difficult to estimate, with spectroscopic methods like partial least squares (PLS) regression, spectral feature analysis (SFA), and multiple endmember spectral mixture analysis (MESMA) typically outperforming hyperspectral indices. Using an independent validation dataset, the lowest root mean squared error (RMSE) values were 0.115 for GV using either normalized difference vegetation index (NDVI) or SFA, 0.164 for NPV using PLS, and 0.126 for soil using PLS. PLS also had the lowest RMSE averaged across all three cover types. This work highlights the need for more extensive and diverse fine spatial scale measurements of fractional cover, to improve methodologies for estimating cover in preparation for future hyperspectral global monitoring missions.

Keywords: fractional cover mapping; field spectroscopy; PRISMA; HISUI; EnMAP; HyspIRI; Surface Biology and Geology (SBG)

1. Introduction

Terrestrial vegetation is dynamic, with both photosynthetically active and inactive vegetation cover varying on seasonal, annual, and decadal time scales. To quantify spatial and temporal variations in vegetation cover, previous studies have modeled cover in natural and agricultural ecosystems as having three fractional components that sum to 100% cover: photosynthesizing or "green" vegetation (GV), non-photosynthesizing vegetation (NPV), and bare soil [1–4]. NPV cover includes dead and senescent leaves and needles, plant litter, and non-photosynthesizing branch and stem tissues. A transition from GV to NPV or soil cover is a hallmark of both seasonal and long-term drought. Grasslands senesce during periods of drought, resulting in a decrease in GV cover and a corresponding increase in NPV cover [5]. Long-term drought can result in canopy dieback and mortality, producing similar changes in fractional cover [6].

Changes in fractional cover also occur with disturbances like insect infestation [7] and wind damage [2]. Senescence and the "curing" of vegetation leads to increased fire danger, and both GV and NPV cover are correlated with fuel moisture content and can be used to measure seasonal changes in fire danger [8]. Changes in NPV cover can indicate the build-up of fine fuel biomass over time [9], while fractional soil cover is closely tied to fire severity [10]. As vegetation regrows following disturbance, GV cover increases and soil cover decreases over time [11].

Fractional cover of GV, NPV, and soil is also important in agricultural systems. In croplands, GV cover typically increases through the growing season, followed by exposure of NPV and soil following harvest. Crop residue is an important form of NPV that can indicate tillage practices used for the management of both soil erosion and carbon flux [12,13]. In rangelands, GV and NPV cover are related to degradation of pastures [14,15] and forage quality [16].

Fractional cover of GV, NPV, and soil have been frequently mapped using linear spectral mixing techniques, either directly (e.g., [17,18]) or through the use of multispectral indices (e.g., [3]). GV cover can be easily estimated from broadband multispectral data due to the distinguishing spectral characteristics of healthy, photosynthesizing vegetation: chlorophyll absorption, the red edge, high near infrared (NIR; 700–1400 nm) reflectance, and liquid water absorption in the shortwave infrared (SWIR, 1400–2500 nm). NPV cover is spectrally distinct from soil due to absorption by non-pigmented organic molecules, primarily lignin and cellulose, but most broadband multispectral sensors are not able to resolve lignocellulose absorption features centered near 2100 and 2300 nm [19].

Hyperspectral sensors (also commonly referred to as imaging spectrometers) have narrow bands (5–10 nm full-width half maximum (FWHM)) capable of fully resolving lignocellulose absorption features, and hyperspectral data have consistently demonstrated more accurate mapping of fractional cover when compared to multispectral data [3,14,17,20]. As a result, a new generation of satellite hyperspectral sensors should improve fractional cover mapping. Hyperspectral missions recently launched or planned for launch over the next several years include the Hyperspectral PRecursor of the Application Mission (PRISMA [21]), the Hyperspectral Imager Suite (HISUI; [22]), and the Environmental Monitoring and Analysis Program (EnMAP; [23]). All of these missions have "VSWIR" sensors covering visible through SWIR wavelengths (approximately 400–2500 nm) and will be tasked due to a limited number of scenes that can be acquired per orbit.

Progress is also being made toward hyperspectral global monitoring missions. The 2007 US National Academies decadal survey on Earth science and applications [24] recommended the Hyperspectral Infrared Imager (HyspIRI) as a Tier 2 mission. HyspIRI was to have a VSWIR instrument and a complementary thermal infrared sensor [25]. The 2017 decadal survey set new priorities for the following decade, with a stronger focus on science and application needs, rather than prioritizing specific missions [26]. Science and application objectives grouped under Surface Biology and Geology (SBG) were designated as priority observation needs, with a VSWIR hyperspectral sensor being the favored measurement approach for addressing those objectives. Based on the heritage design from HyspIRI and SBG observation requirements, a future hyperspectral global monitoring mission can be projected to have 30 m spatial resolution, 380–2500 nm spectral range with 10 nm FWHM bands, and a

16-day revisit period [25,26]. Beyond a mission based on SBG observation requirements, there is also potential for hyperspectral sensors on Landsat and Sentinel missions in the late 2020s [27,28].

With the advent of these new hyperspectral sensors and the continuing need for fractional cover information, more assessment of the potential accuracy of spectroscopic GV, NPV, and soil fractional cover estimates is required [29]. As fractional cover could be a global "Level 3" product from a future mission based on SBG observation requirements, quantitative comparisons of methods for deriving fractional cover from reflectance spectra are also needed. This paper uses in situ collected field spectra with corresponding fractional cover estimates based on field photography or geometry to simulate VSWIR hyperspectral imager spectra. Our objectives are to use these simulated VSWIR spectra to evaluate competing methods for estimating GV, NPV, and soil fractional cover from hyperspectral data, and to compare the potential accuracy of each method.

2. Materials and Methods

2.1. Simulated VSWIR Spectra

Field spectra collected in six separate prior experiments were used to simulate spectra measured by a VSWIR satellite imaging spectrometer. Each field spectrum in these datasets has a corresponding fractional cover of GV, NPV, and/or soil determined from field photography or geometry. All reflectance spectra in the field experiments described below were measured using Analytical Spectral Devices (ASD) field spectrometers (ASD Incorporated/Malvern Panalytical, Westborough, MA, USA). The native sampling intervals of ASD spectrometers range from approximately 1.4 nm for the visible/near-infrared detector (VNIR; 350 to 1000 nm) to approximately 2.2 nm for the SWIR detectors (1001 to 2500 nm). ASD instruments resample the native channels using cubic spline interpolation before recording 2151 channels at standardized wavelengths (350 to 2500 nm) at a 1 nm interval [30]. The spectral bandpass of ASD spectrometers vary across the wavelength range of each detector and differs between spectrometer models, ranging from approximately 3 to 12 nm [31].

Daughtry and Hunt [32] collected 600 field spectra from seven different agricultural field sites near Beltsville, Maryland, USA. These spectra captured fields with varying cover of soil, crop residue, and young corn, soybean, or wheat plants. The 18° foreoptic of an ASD FieldSpec Pro spectrometer was mounted alongside a digital camera on a pole at 2.3 m above the surface with a 0° view zenith angle. Photographs of the spectrometer field-of-view were overlain by a matrix of 156 points, and visual interpretation was used to assign each point as GV, NPV, or soil. Fractional cover for each spectrum was determined by dividing the number of points in each class by the total number of points. These spectra and fractional cover estimates will be referred to in this paper as "DH-crop".

A second agricultural dataset included only NPV and soil cover, and was derived from Quemada and Daughtry [33]. An ASD FieldSpec 3 with an 18° foreoptic was used to measure the reflectance of soil and crop residue mixtures for a field near Beltsville. Crop residue cover and moisture conditions were manually manipulated in a series of experiments carried out on three different dates. Both the spectrometer foreoptic and a digital camera were mounted on a pole at 2.3 m above the surface at a 0° view zenith angle. Photographs of the spectrometer field-of-view were overlain by a matrix of 132 points, and visual interpretation was used to assign each point as NPV or soil. As with DH-crop, fractional cover was determined by dividing the number of points in each class by the total number of points. Relative water content (RWC) of soil and residue was measured for all spectra. Spectra of material with RWC in excess of 60% were excluded from this analysis due to strong SWIR darkening, providing a total of 410 spectra and associated NPV-soil fractional cover values. These spectra and fractional cover estimates will be referred to in this paper as "QD-crop".

A dataset including only GV and NPV cover was derived from time series grassland spectra collected at Coal Oil Point near Goleta, California, USA. Spectra were measured at 12 plots from December 2015, through the following May, with an average interval between measurements of 17 days, providing a total of 129 spectra. An ASD FieldSpec 4 with no foreoptic (25° field-of-view) was placed in

a sample frame to measure the same field-of-view on each date. A digital camera was placed over the same sampling frame to take a photograph of the spectrometer field-of-view. Both the fiber and camera were mounted on a tripod at 1.05 m above the surface and a 0° view zenith angle. A decision tree classifier, trained on multiple years of images collected at this location, was applied to each photograph to classify the red, green, and blue digital number values of each photograph pixel into GV, NPV, and shadow classes. To calculate fractional cover of GV and NPV, the number of pixels in each class was divided by the sum of pixels in the GV and NPV classes, thus excluding shadowed pixels. These spectra and fractional cover estimates will be referred to in this paper as "CA-grass".

A second dataset containing only GV and NPV cover was derived from grassland spectra acquired at six sites in Rondônia, Brazil by Numata et al. [14]. An ASD Full Range spectrometer with no foreoptic (22° field-of-view) was used to measure spectra every 5 m along 100 m transects, with a height of 1 m above the surface. Each field-of-view was photographed, and photographs were digitally decomposed into GV, NPV+Soil, and shadow classes using empirically determined red, green, and blue digital number value thresholds [14]. This method was unable to separate NPV and soil cover, so for this paper, all field photographs were visually inspected for partial soil cover and spectra containing any suspected soil cover were discarded. Cover fractions for the remaining 60 spectra were normalized to remove shadow. These spectra and fractional cover estimates will be referred to in this paper as "RO-grass".

A dataset containing time series shrub spectra was collected from coastal southern California and the University of California Sedgwick Reserve, both in Santa Barbara County, California, USA [34]. Measured species included evergreen broadleaf shrubs *Arctostaphylos glauca*, *Baccharis pilularis*, *Ceanothus cuneatus*, and *Ceanothus megacarpus*; drought-deciduous broadleaf shrubs *Artemisia californica* and *Salvia leucophylla*; and evergreen needleleaf shrub *Adenostoma fasciculatum*. This dataset contained only GV and NPV cover. Spectra were measured approximately every two weeks for a year, starting in April 2011, with some gaps in temporal coverage. An ASD Full Range field spectrometer with no foreoptic (24° field-of-view) was used to measure the sunlit side of individual shrub canopies from a height of approximately 1 m above the canopy. The same shrub canopies were revisited on each date. Each field-of-view was photographed, with GV and NPV fractional cover estimated using the same method as for CA-grass. The 595 spectra and fractional cover estimates from this dataset will be referred to in this paper as "CA-shrub".

The final dataset providing only GV and soil cover was derived from spectra collected over a resprouting clonal *Populus* stand near Wallula, Washington, USA [35,36]. Resprouting trees ranged between 10 cm and 60 cm in height. Spectra were measured using an ASD Full Range spectrometer with no foreoptic (24° field-of-view) with a height of 0.5 m above each canopy. Leaf area index (LAI) was measured using destructive harvesting and ranged from 1.8 to 8.75 [35]. Percent cover of GV and soil was determined geometrically, by measuring the semi-major and semi-minor axis of each canopy, calculating the elliptical canopy area, and then dividing by the area of the field-of-view. Of twenty-four spectra collected, twenty had complete GV cover and four had GV cover ranging from 57% to 84%. These spectra and fractional cover estimates will be referred to in this paper as "WA-tree".

All reflectance spectra were convolved to 10 nm bands to approximate the anticipated bandpass function of a VSWIR instrument satisfying anticipated SBG observation requirements [26]. The synthetic bands used centers spaced every 10 nm between 400 and 2500 nm, and a 10 nm Gaussian FWHM. To make the simulated spectra a better approximation of spectra measured by a satellite sensor, the 10 nm reflectance spectra were converted to radiance using a lookup table generated using MODTRAN 5.3 [37], radiance-dependent sensor noise was added, and then reflectance was retrieved from the resulting radiance spectra. The MODTRAN simulations varied reflectance between 0 and 70% at a 0.1% interval, and assumed a 30° solar zenith angle, 2 cm column water vapor, and 30 km visibility for a standard mid-latitude summer atmospheric profile with rural aerosol scattering. Based on the reflectance value in each band, radiance was spline interpolated from the radiance values in the lookup table. At the time of this study, the instrument or instruments selected to implement SBG measurement objectives

are not yet known. Consequently, we used a HyspIRI VSWIR spectrometer design as a conservative performance bound to apply instrument noise to the radiance spectra. The radiance-dependent noise function was based on a comprehensive model of the HyspIRI VSWIR spectrometer design, with instrument photon throughput and all significant noise sources including detector, photon, and read noise for each band (R. Green, personal communication). Using the noise function, Gaussian noise was added to each spectrum [38]. Finally, the spectra were processed through a variant of the ATREM code (ATmospheric REMoval) currently used for Airborne Visible InfraRed Imaging Spectrometer (AVIRIS) data [39].

The resulting reflectance spectra approximate products from a satellite imaging spectrometer, complete with noise and atmospheric correction residuals. Figure 1 compares an original 1 nm field spectrum to a simulated 10 nm VSWIR spectrum. Bands on the edge of major atmospheric water vapor absorption features, shown in black, were not used for further analysis. Residuals caused by atmospheric correction were similar across all spectra, since the same MODTRAN model atmosphere and the same input parameters for ATREM were used across the entire library. The residuals shown in Figure 1 resemble residuals frequently seen in AVIRIS reflectance data, and presumably will be present in some form in future hyperspectral satellite reflectance products. In an actual global hyperspectral dataset, spatial variation in atmospheric correction residuals would be an additional source of error. All field reflectance spectra convolved to the 10 nm bandpass function [40] and simulated VSWIR spectra including noise and atmospheric correction residuals [41] have been made available as spectral libraries with full metadata on the Ecosystem Spectral Information System (EcoSIS; [42]).
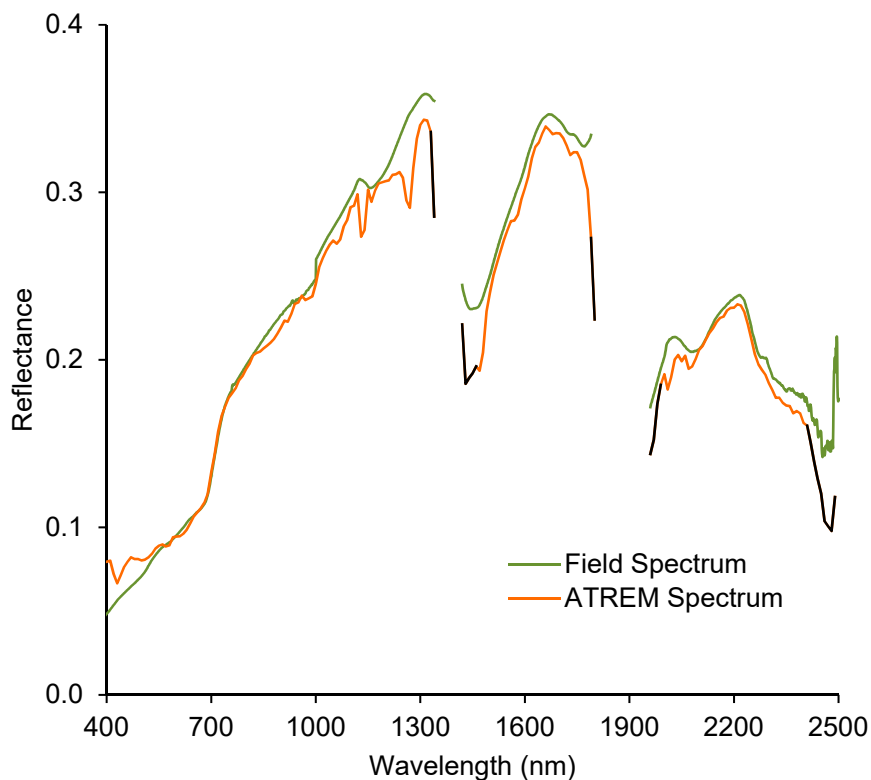

Figure 1. A single 1 nm oversampled field spectrum (green) processed to a simulated 10 nm bandwidth VSWIR spectrum (orange). Bands excluded due to proximity to atmospheric water vapor absorption features are shaded black. VSWIR includes the visible, near infrared, and shortwave infrared spectral regions.

We designed the error assessment for fractional cover estimation in this study to resemble hypothetical error assessment for global fractional cover mapping by using separate spatial and temporal subsets of the VSWIR spectral library for algorithm training and validation. Random

assignment of data into training and validation subsets could inflate accuracy compared to real-world application, since spectra from each prior experiment are not independent observations, but rather are correlated in space and in time. To provide a more rigorous assessment of error for each fractional cover metric described in Section 2.2, the simulated VSWIR spectral library was split and assigned into training and validation subsets using primarily spatial or temporal criteria. The DH-crop and RO-grass spectra were split by site. For DH-crop, four sites (345 spectra) were assigned to the training subset and three sites (255 spectra) were assigned to the validation subset. The single site with the highest diversity in fractional cover was purposefully put into the training subset to provide a more robust training spectral library. For RO-grass, three sites (33 spectra) were assigned to the training subset and three sites (27 spectra) were assigned to the validation subset. QD-crop, CA-grass, and CA-shrub spectra were split by date. For QD-crop, the first two dates/moisture treatments (214 spectra) were added to the training subset and the final date/moisture treatment (102 spectra) was added to the validation subset. For CA-grass, the date of peak greenness was determined across all twelve sites, and all spectra preceding and including that date (72 spectra), representing the green-up period, were assigned to the training subset. All spectra following that date (57 spectra), representing the dry-down period, were assigned to the validation subset. For CA-shrub, 349 "greenup season" spectra within the months of January–June were placed in the training subset. The remaining 246 "dry season" spectra within the months of August–December were placed in the validation subset. Finally, the WA-tree spectra were randomly and equally split into the training and validation subsets, due to the small number of spectra (24) and single site/single date collection. The subset with greater variation in fractional cover was assigned as the training subset.

Across all six contributing datasets, the training library totaled 1025 spectra and the validation library totaled 698 spectra, providing an approximate 60/40% split between training and validation data. Training and validation sets were not equivalently distributed across fractional cover space, however. Figure 2 displays ternary diagrams representing the fractional cover of each spectrum in the training (Figure 2a) and validation (Figure 2b) libraries. Only the DH-crop dataset had all three cover types, with the other datasets falling along the NPV-GV, NPV-soil, or GV-soil axes. The NPV-GV axis had the densest coverage due to three datasets (RO-grass, CA-grass, and CA-shrub) missing soil cover. The validation library had fewer spectra with high GV fraction and with GV-soil mixtures compared to the training library (Figure 2).

2.2. Hyperspectral Fractional Cover Metrics

Two broad categories of hyperspectral metrics were tested for their ability to estimate GV, NPV, and soil fractional cover: indices and spectroscopic methods. The hyperspectral indices evaluated in this study all used two or three individual bands, while three spectroscopic methods used a large number of contiguous bands. Indices were calculated for training library spectra, and then linear or quadratic functions were used to determine the best-fit relationship between each index and fractional cover. The best-fit function for each index was applied to the spectra in the independent validation library. The spectroscopic methods were trained using training library spectra as described below and then used to predict fractional cover from the validation library spectra. For both indices and spectroscopic methods, fractional cover predicted from the validation library spectra was compared to the actual fractional cover.

Traditional red-NIR vegetation indices are strongly correlated with GV fractional cover [43,44]. For this study, three standard vegetation indices were used to estimate GV fractional cover: NDVI, EVI, and NDII (abbreviations defined in Table 1). NDVI relies on spectral contrast between chlorophyll absorption and NIR reflectance [45], with EVI adding correction factors to account for variation in background brightness and reducing the impacts of aerosol scattering through the use of a blue band [46]. NDII relies on canopy liquid water absorption in the SWIR [47]. All three indices increase as GV cover increases. Additional vegetation indices were also tested, including multiple variants of

the soil adjusted vegetation index (SAVI) [48]. We have included results for these additional indices in the supplemental materials for this paper.

For each reflectance term listed in Table 1, the 10 nm band centered on the indicated wavelength was used to calculate each index. NDVI used a reflectance minimum at 670 nm for the red band, while EVI used the approximate MODIS band center at 650 nm. Each index was regressed against the GV fraction from the training library, and fit with a second degree polynomial function due to the saturation of these indices with increasing LAI [49,50]. The best-fit quadratic equation was used to predict GV fraction from the validation spectral library.
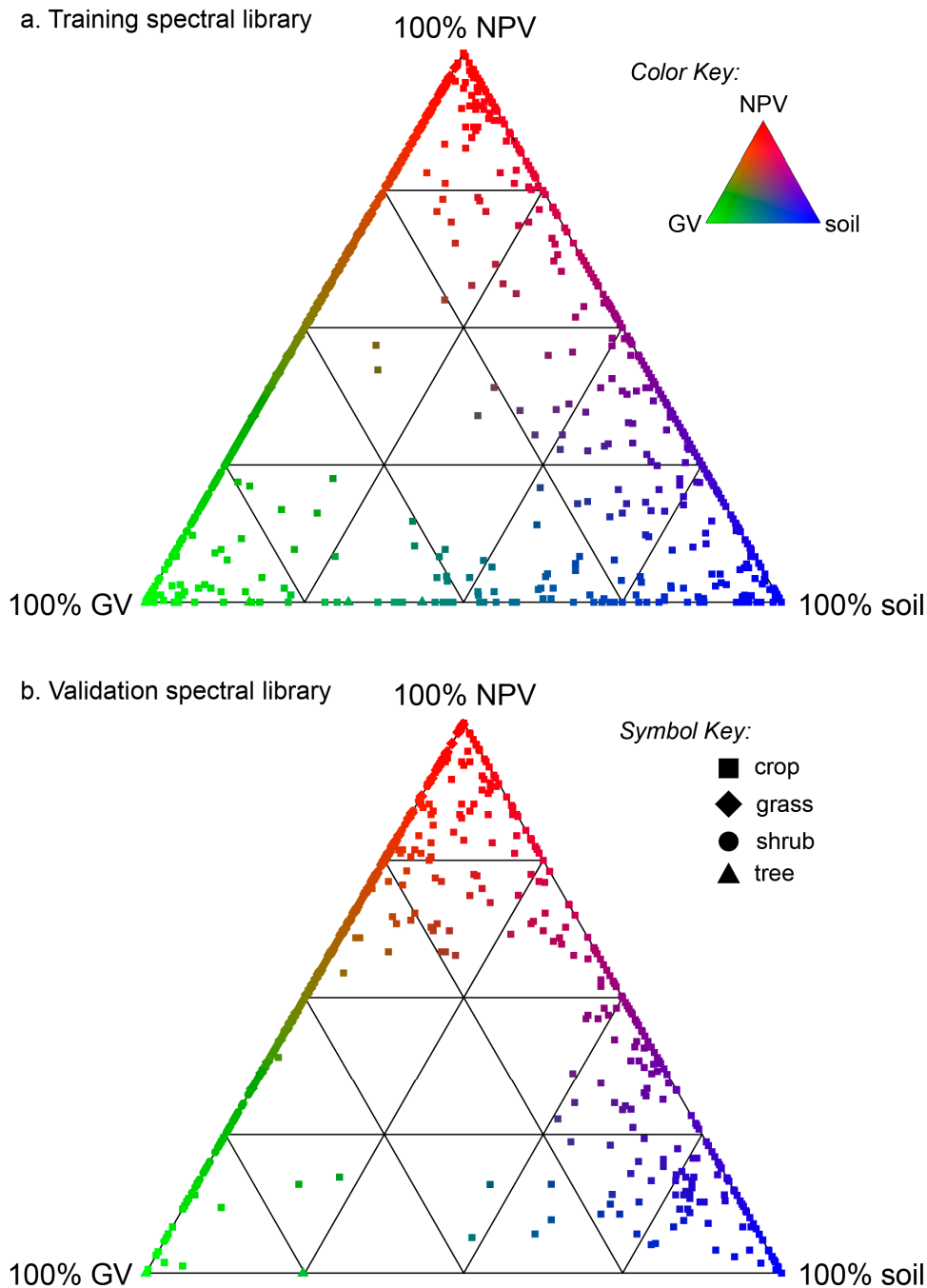

Figure 2. Ternary plots for the (**a**) training and (**b**) validation spectral libraries. Both position on the plot and color indicate the fractional cover for each cover type. The color and symbol keys apply to both plots.

We used three indices developed for direct measurement of lignocellulose absorption expressed by NPV cover (Table 2). CAI was developed to contrast lignocellulose absorption at 2100 nm with two reference bands at 2000 and 2200 nm [51,52]. We used wavelengths further refined by Serbin et al. [53] to take advantage of 10 nm bandwidth and avoid the effects of carbon dioxide absorption closer to 2000 nm (Table 2). Both ligno-cellulose absorption index (LCA) and the SWIR normalized residue index (SINDRI) were developed for Advanced Spaceborne Thermal Emission and Reflection Radiometer (ASTER) bands, and thus were not optimized for capturing lignocellulose absorption [54,55]. We used ASTER band centers for LCA, and the hyperspectral version of SINDRI (hSINDRI) described in Serbin et al. [55]. The best-fit linear function between each index and NPV fractional cover was applied to the spectra from the validation library.

Table 1. Metrics related to green vegetation (GV) fractional cover. ρ is reflectance; all subscript numbers are wavelengths in nm.

Metric	Full Name	Formula	References
NDVI	normalized difference vegetation index	$\frac{\rho_{860}-\rho_{670}}{\rho_{860}+\rho_{670}}$	[45]
EVI	enhanced vegetation index	$2.5\times\frac{\rho_{860}-\rho_{650}}{\rho_{860}+6\times\rho_{650}-7.5\times\rho_{470}+1}$	[46]
NDII	normalized difference infrared index	$\frac{\rho_{860}-\rho_{2130}}{\rho_{860}+\rho_{2130}}$	[47]
SFA	spectral feature analysis	$area_{670\text{nm}} = area_{below} - area_{above}$, where $area_{below}$ and $area_{above}$ are relative to the continuum line using endpoints at 540 and 760 nm	[56]
MESMA	multiple endmember spectral mixture analysis		[57]
PLS	partial least squares regression		[58]

Table 2. Metrics related to non-photosynthetic vegetation (NPV) fractional cover. ρ is reflectance; all subscript numbers are wavelengths in nm.

Metric	Full Name	Formula	References
CAI	cellulose absorption index	$0.5\times(\rho_{2030}+\rho_{2210})-\rho_{2100}$	[53]
LCA	ligno-cellulose absorption index	$(\rho_{2200}-\rho_{2160})+(\rho_{2200}-\rho_{2330})$	[54]
hSINDRI	hyperspectral SWIR normalized residue index	$\frac{\rho_{2210}-\rho_{2260}}{\rho_{2210}+\rho_{2260}}$	[55]
SFA	spectral feature analysis	$area_{2100\text{nm}} = area_{below} - area_{above}$, where $area_{below}$ and $area_{above}$ are relative to the continuum line using endpoints at 2040 and 2210 nm	[56]
MESMA	multiple endmember spectral mixture analysis		[57]
PLS	partial least squares regression		[58]

Soil does not have characteristic absorption features like GV (chlorophyll) or NPV (lignin and cellulose). Soil spectra may express many different mineral absorptions, or none at all in the VSWIR wavelengths [59], so no single index was available to apply to the spectral libraries used in this study. Instead, the indices with the lowest RMSE for predicting validation library GV and NPV fractional cover were used to create a narrowband index soil approximation (Table 3). This metric was calculated

as $1 - (GV_{NDVI} + NPV_{CAI})$, where GV_{NDVI} is GV cover estimated using the best-fit polynomial function for NDVI and NPV_{CAI} is NPV cover estimated using the best-fit linear function for CAI.

Table 3. Metrics related to soil fractional cover.

Metric	Full Name
$1 - (GV_{NDVI} + NPV_{CAI})$	narrowband index soil approximation
$1 - (GV_{SFA} + NPV_{SFA})$	SFA soil approximation
MESMA	multiple endmember spectral mixture analysis
PLS	partial least squares regression

Spectral feature analysis (SFA) with continuum removal was applied to selected absorption features for estimating GV and NPV fractional cover, including the 670 nm chlorophyll absorption feature to estimate GV cover (Table 1) and the 2100 nm lignocellulose feature to estimate NPV cover (Table 2). A second lignocellulose absorption feature at 2300 nm has been previously linked to plant biochemical composition [60,61], but the 2100 nm feature was selected for use with SFA due to higher signal-to-noise in the simulated VSWIR spectra. Continuum removal is a method used to isolate and remove the influence of the other absorptions present in the spectrum, not including the absorption feature of interest [62]. In linear continuum removal, the continuum is defined by the line connecting bands at points on the left and right sides of an absorption feature. Area between the spectrum and the continuum line, both above (*area*$_{above}$) and below (*area*$_{below}$) the line, can be calculated, using the continuum line to normalize the reflectance values [56]. Parameters such as feature depth and area have been correlated with the amount or concentration of an absorbing chemical [56,60].

Since the spectra analyzed in this study included the full range of GV and NPV cover, including spectra containing no GV or NPV cover, some spectra did not have absorption features at 670 and 2100 nm and reflectance could exceed the continuum line. To account for area both above and below the continuum line, net area was calculated as *area*$_{below}$ − *area*$_{above}$. This net area has higher positive values when an absorber in the continuum range is present, and allows for negative values when an absorber is not present and spectral shape leads to a net area above the continuum line.

The two net area metrics, *area*$_{670nm}$ and *area*$_{2100nm}$, were calculated using USGS Processing Routines in IDL for Spectroscopic Measurements (PRISM) software [63]. Both net area metrics were calculated for the training spectral library, and then regressed against GV cover and NPV cover respectively, using a second-degree polynomial model for GV and a linear model for NPV. The resulting regression coefficients were then applied to the validation spectral library to predict both GV and NPV fractional cover. Similar to spectral indices, SFA was unable to directly estimate soil cover due to the lack of a characteristic absorption feature. To approximate soil fractional cover for the validation library using SFA, the sum of SFA-estimated GV cover (SFA$_{GV}$) and NPV cover (SFA-$_{NPV}$) was subtracted from one (Table 3).

The final two metrics used the entire VSWIR spectrum from 400 to 2500 nm, excepting the water vapor influenced bands shown in black in Figure 1. Multiple endmember spectral mixture analysis (MESMA; [57]) was used to directly estimate GV, NPV, and soil fractional cover based on linear mixtures of selected endmembers. MESMA is an extension of spectral mixture analysis, which uses a fixed set of endmembers to model fractional cover within a pixel [1]. Each endmember represents a particular type of pure cover, and each pixel or spectrum is modeled as a linear combination of those endmembers. Endmember fractions are constrained to sum to one. Unlike simple spectral mixture analysis, MESMA allows the number and identity of endmembers to change, such that multiple spectra could represent pure GV, NPV, or soil cover. We used three- and four-endmember mixing models, where each model consisted of a photometric shade endmember and two or three non-shade endmembers taken from GV, NPV, and soil cover types. MESMA assigns the best-fit mixing model and the resulting estimated cover fractions to each modeled spectrum. For comparison with field-assessed fractional cover data, fractions estimated by MESMA are shade normalized, dividing each fraction by the sum of the non-shade

fractions. MESMA has been widely used to model sub-pixel fractional cover using multispectral and hyperspectral data [64].

Endmember selection is typically the most effort-requiring step for fractional cover modeling using MESMA, since different endmember libraries can result in large differences in predicted fractional cover. Local investigations typically achieve the best performance by developing endmember libraries that capture variability in specific species, vegetation condition, and terrain [64]. For use on pooled data from six datasets using spatial and temporal subsets, we developed a more generic approach that selects optimal endmember models, rather than optimal endmembers. First, potential endmembers were selected from the training library by requiring at least 95% fractional cover in one of the three cover types. The endmember average RMSE (EAR) technique, as described by [65,66] and implemented in ViperTools [67], was used to find the most six most representative GV, NPV, and soil endmembers from the training library. Three- and four-endmember mixing models, where each model consisted of a photometric shade endmember and two or three non-shade endmembers, were then used to model the training library. Endmember fractions were constrained to between −10% and 110%. Six endmembers for each cover type provided a total of 324 unique mixing models: 36 GV-NPV-shade models, 36 NPV-soil-shade models, 36 GV-soil-shade models, and 216 GV-NPV-soil-shade models. An iterative approach [68,69] was used to select the individual three- and four-endmember mixing models that most accurately estimated cover fractions in the training library. Models were iteratively added to and subtracted from a model list, and changes to the model list that resulted in the largest improvement in mean fraction RMSE were retained. This process selected 29 individual mixing models before mean RMSE could no longer be improved, including six GV-NPV-shade models, nine NPV-soil-shade models, seven GV-soil-shade models, and seven GV-NPV-soil-shade models. The model set selected from the training library was then applied to the validation library, and the best-fit model was used to assign an estimated fractional cover to each spectrum. Modeled fractions were shade normalized, dividing each fraction by the sum of the non-shade fractions. Due to shade normalization, the final fractional cover modeled by MESMA could be outside the range of −10% to 110%.

Partial least squares regression (PLS) was the final spectroscopic method used to estimate GV, NPV, and soil fractional cover. PLS uses orthogonal projection to create latent vectors (components) that model the relationship between fractional cover and spectral reflectance, and is an appropriate method for dealing with the multicollinearity inherent in hyperspectral reflectance data [70]. PLS has been widely applied in remote sensing to estimate plant biochemical constituents [71–73]. The R package *pls* [58] was used to construct a separate single-response PLS model for each cover type. Overfitting using an inflated number of components is a concern for PLS, and as a result our models were trained using subsets of the training library. Eighty percent of the training library was selected over 100 iterations, and model fit was determined using leave-one-out validation for each training library subset. The optimal number of components was determined when the prediction residual sum of squares (PRESS) was minimized, and successive components did not improve RMSE as assessed using a t-test. Once the optimal number of components was determined, a final PLS model was created using the entire training library, and the model was subsequently applied to the validation library using the same number of components.

Based on the metrics described above and in Tables 1–3, predicted cover fractions were compared to actual cover fractions for the 698 spectra in the validation library. No attempt was made to correct predicted fractional cover that was less than zero or that exceeded one. RMSE was calculated for each metric, and a best-fit linear function was used to calculate the coefficient of determination (R^2).

3. Results

GV fractional cover was estimated with lower error in comparison to NPV and soil fractional cover (Table 4). Due to the spectral distinctiveness of GV cover, both simple indices and spectroscopic methods performed relatively well in predicting fractional cover. NDVI, one of the most basic

vegetation indices, and SFA, a spectroscopic method focusing solely on a chlorophyll absorption feature in this case, outperformed the other metrics when applied to the validation library. Plots comparing predicted and actual GV fractions from the validation library demonstrate underestimation of GV fraction at the highest levels of fractional cover (Figure 3), with the exceptions of MESMA (Figure 3e) and PLS (Figure 3f). High GV fraction spectra were a relatively small percentage of the training library, and lower representation combined with the non-linear relationship between metrics and chlorophyll absorption are likely responsible for underestimation of GV. NDVI and EVI performed similarly at intermediate GV fractional cover (Figure 3a,b). At high GV cover, EVI was better able to account for saturation effects, but at very low GV cover, EVI produced higher error in estimated GV fractions, in balance resulting in higher RMSE.

Table 4. Root mean squared error (RMSE) and R^2 values for fractional cover metrics, ordered by cover type and then from lowest to highest validation library RMSE.

Cover Type	Metric	Training		Validation	
		RMSE	R^2	RMSE	R^2
GV	NDVI	0.115	0.865	0.115	0.845
GV	SFA	0.108	0.880	0.115	0.841
GV	PLS	0.075	0.942	0.125	0.807
GV	EVI	0.133	0.817	0.130	0.794
GV	NDII	0.138	0.805	0.147	0.753
GV	MESMA	0.136	0.846	0.149	0.793
NPV	PLS	0.102	0.873	0.164	0.641
NPV	SFA	0.175	0.627	0.176	0.587
NPV	CAI	0.187	0.572	0.177	0.618
NPV	MESMA	0.159	0.711	0.181	0.592
NPV	LCA	0.201	0.509	0.211	0.476
NPV	hSINDRI	0.261	0.167	0.256	0.157
Soil	PLS	0.089	0.933	0.126	0.850
Soil	MESMA	0.144	0.831	0.135	0.832
Soil	$1 - (GV_{NDVI} + NPV_{CAI})$	0.197	0.736	0.141	0.870
Soil	$1 - (GV_{SFA} + NPV_{SFA})$	0.175	0.748	0.167	0.804

NPV fractional cover had higher validation RMSE values than GV or soil (Table 4). PLS had the lowest validation RMSE for NPV. SFA and CAI, both based on the 2100 nm lignocellulose absorption feature, produced similar NPV validation RMSE values, but demonstrated very different errors when plotted (Figure 4). CAI, LCA, and hSINDRI overestimated NPV fraction for spectra possessing high GV fraction (Figure 4a–c). hSINDRI demonstrated a particularly poor relationship between predicted and actual NPV fraction (Table 4, Figure 4c). All four metrics based solely on lignocellulose absorption tended to underestimate NPV cover at the highest fractions, while MESMA and PLS did not demonstrate this tendency.

Unlike other metrics, the MESMA mixing models we created could explicitly exclude one of the cover types when modeling a spectrum. For example, a mixture of GV and NPV with no soil could be modeled by a three-endmember model consisting only of a GV endmember, an NPV endmember, and a shade endmember. Discriminating NPV and soil at low fractional cover is difficult, however, and MESMA sometimes chose an incorrect three endmember model. Figure 4e demonstrates that several crop spectra with no actual NPV cover were assigned a best-fit model including an NPV endmember, when a three-endmember model including no NPV endmember would have been more appropriate.
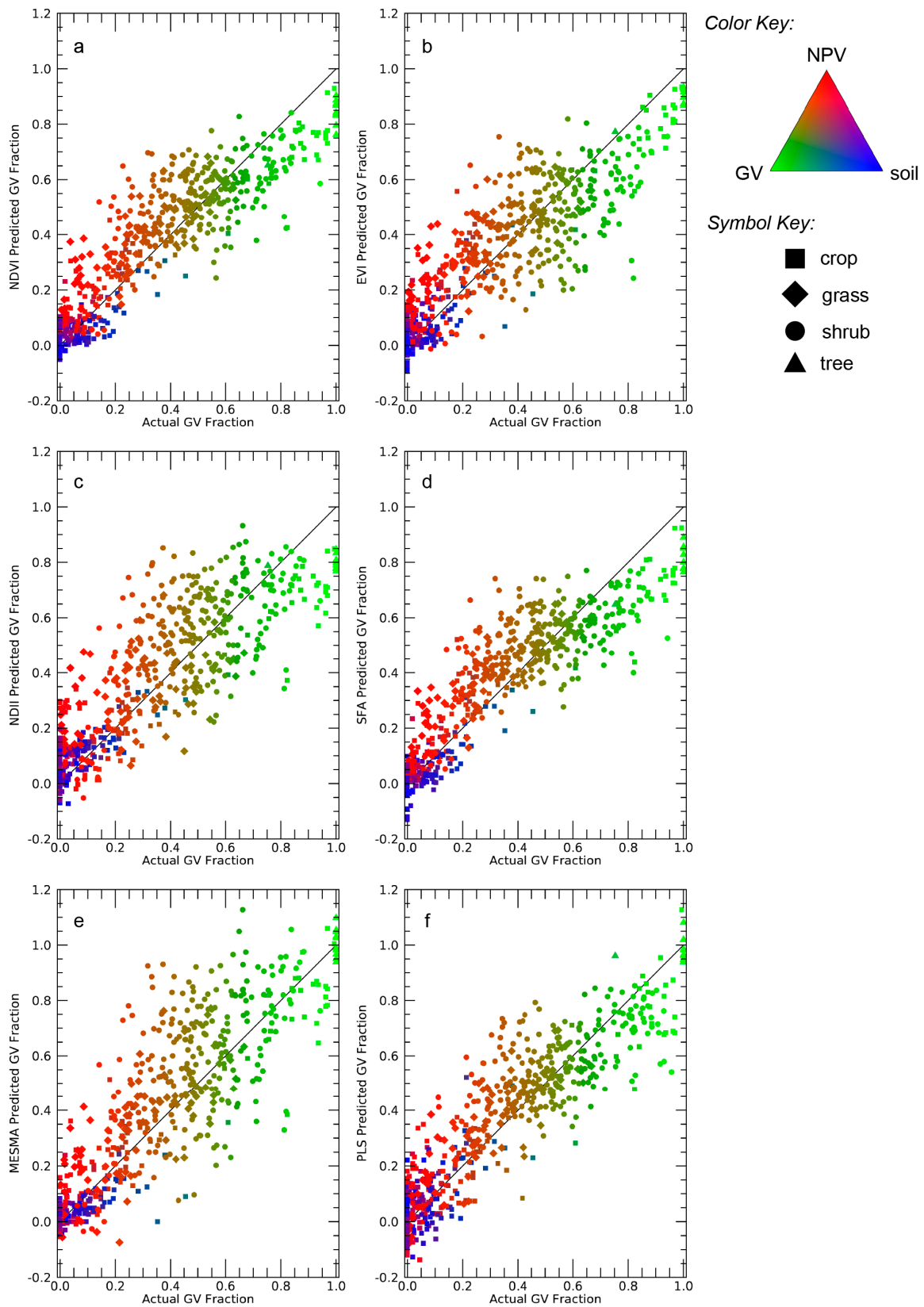
Figure 3. Actual vs. predicted green vegetation (GV) fractional cover for the validation library for (**a**) NDVI, (**b**) EVI, (**c**) NDII, (**d**) SFA, (**e**) MESMA, and (**f**) PLS. See Table 1 for metric definitions. The color of each point indicates the actual GV, NPV, and soil fraction. The diagonal line is a 1:1 ratio and the symbol indicates the vegetation type in the source dataset.
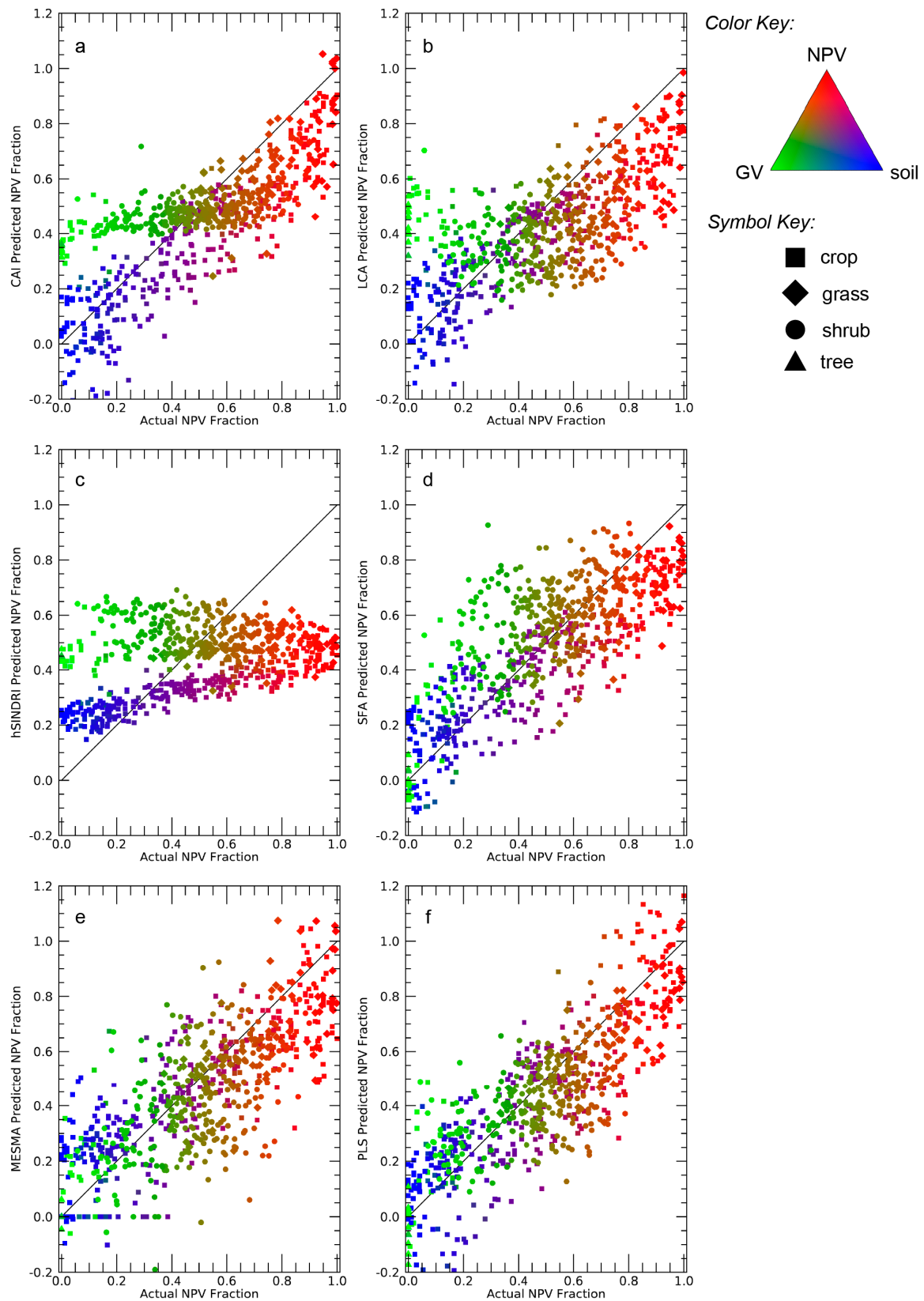
Figure 4. Actual vs. predicted non-photosynthetic vegetation (NPV) fractional cover for the validation library for (**a**) CAI, (**b**) LCA, (**c**) hSINDRI, (**d**) SFA, (**e**) MESMA, and (**f**) PLS. See Table 2 for metric definitions. The color of each point indicates the actual GV, NPV, and soil fraction. The diagonal line is a 1:1 ratio and the symbol indicates the vegetation type in the source dataset.

Soil fractions were estimated with lower validation RMSE than NPV, but soil error values should be viewed cautiously. Forty-four percent of the training library spectra and 47% of the validation library spectra contained no soil cover, resulting in a large spread of predicted soil fraction values at the lowest end of actual soil fraction values (Figure 5). Relatively poorer representation of soil also likely improved model fits over the training data for all metrics except PLS (Table 4). PLS had the lowest validation RMSE for soil. Both the index and SFA approximations overestimated soil fractions below 0.5, while MESMA and PLS did not show a systematic bias.

Figure 5. Actual vs. predicted soil fractional cover for the validation library for (**a**) $1 - (GV_{NDVI} + NPV_{CAI})$, (**b**) $1 - (GV_{SFA} + NPV_{SFA})$, (**c**) MESMA, and (**d**) PLS. The color of each point indicates the actual GV, NPV, and soil. The diagonal line is a 1:1 ratio the symbol indicates the vegetation type in the source dataset.

Across all three cover types, PLS had the lowest average validation RMSE (0.138). Index-based methods had the next lowest average validation RMSE (0.146), with the caveat that CAI demonstrated poor performance on spectra with high GV cover, which were underrepresented in our analysis. SFA (0.153) and MESMA (0.155) had similar average RMSE across all three cover types. While PLS showed the best performance in distinguishing NPV and soil, PLS was not without issues. A large number of latent components, 57 for GV and soil and 99 for NPV, resulted from the training library. PLS coefficients picked up some important spectral features, including higher weightings for visible, red edge, and NIR wavelengths for predicting GV fractions and a high weighting for a 1730 nm

feature associated with lignocellulose for predicting NPV fractions (Figure 6). Other spectral features highlighted by the PLS coefficients make less intuitive sense, like a peak for NPV at 660 nm near the chlorophyll absorption maximum. Difficult-to-interpret coefficient spectra is a common outcome of PLS [72,73], although high frequency variation in our coefficients may indicate that overfitting was still occurring despite our efforts to minimize it.
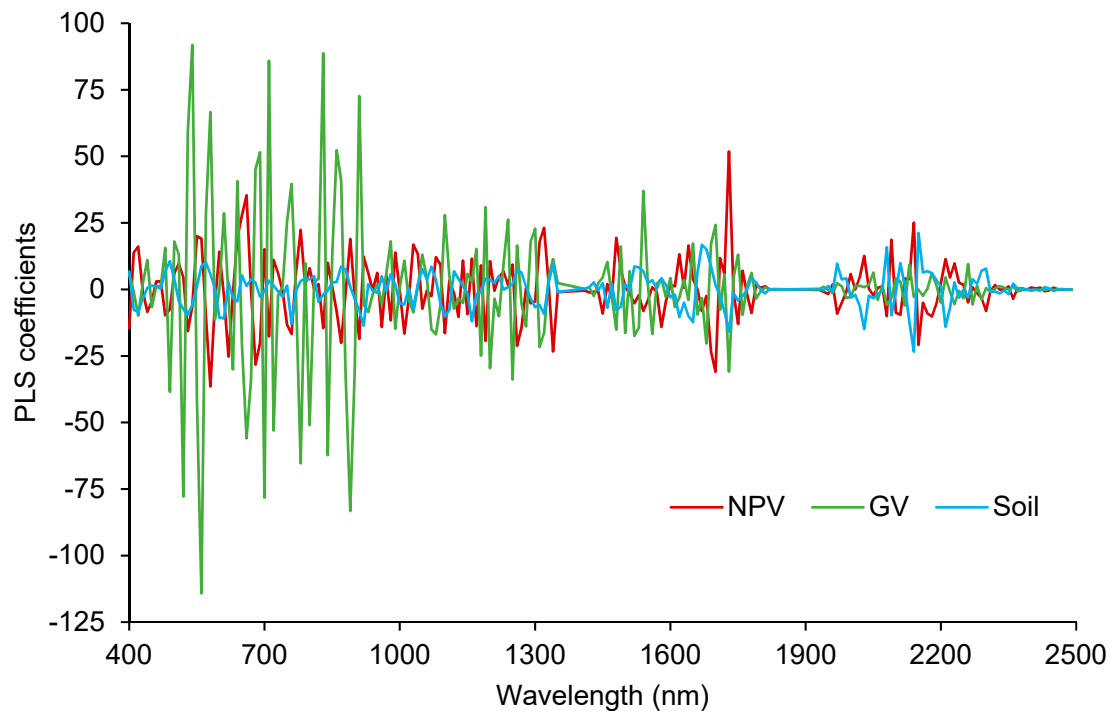

Figure 6. Partial least squares regression coefficients for GV, NPV, and soil fraction models.

4. Discussion

Our results demonstrated that spectroscopic methods like PLS, SFA, and MESMA have advantages over simple hyperspectral indices, including in many cases lower RMSE and improved ability to estimate GV and NPV fractional cover at extreme high values. The gap between spectroscopic methods and spectral index performance was relatively small for GV cover, since spectral features associated with GV cover are much more distinct than the spectral features that allow for separation of NPV and soil. Spectral indices, even those using narrow bands optimized for lignocellulose absorption, were less accurate for estimating NPV fractions than spectroscopic measures such as SFA and PLS. Spectra with elevated GV fractions were particularly problematic for spectral indices associated with NPV. Figure 7 shows an example comparison of two spectra with very different actual fractional cover but similar CAI values. DH-crop spectrum "SF_032" was 12% NPV, 88% GV, and 0% soil. A second spectrum from the same dataset, "SF_101," was more characteristic of a moderate NPV cover spectrum with 65% NPV, 29% GV, and 6% soil. Visible, NIR, and SWIR reflectance are broadly different in this example, but CAI values were essentially the same (0.00743 for SF_032 and 0.00795 for SF_101). CAI underestimated NPV fraction by 10% for SF_101, but due to similar relative reflectances, overestimated NPV fraction by 43% for SF_032. Use of additional spectral information, including reflectance across the visible, NIR, and SWIR, can clearly distinguish that SF_032 does not have moderate NPV cover. To accurately predict NPV fractional cover across the full range of GV cover, a spectroscopic method should be used.
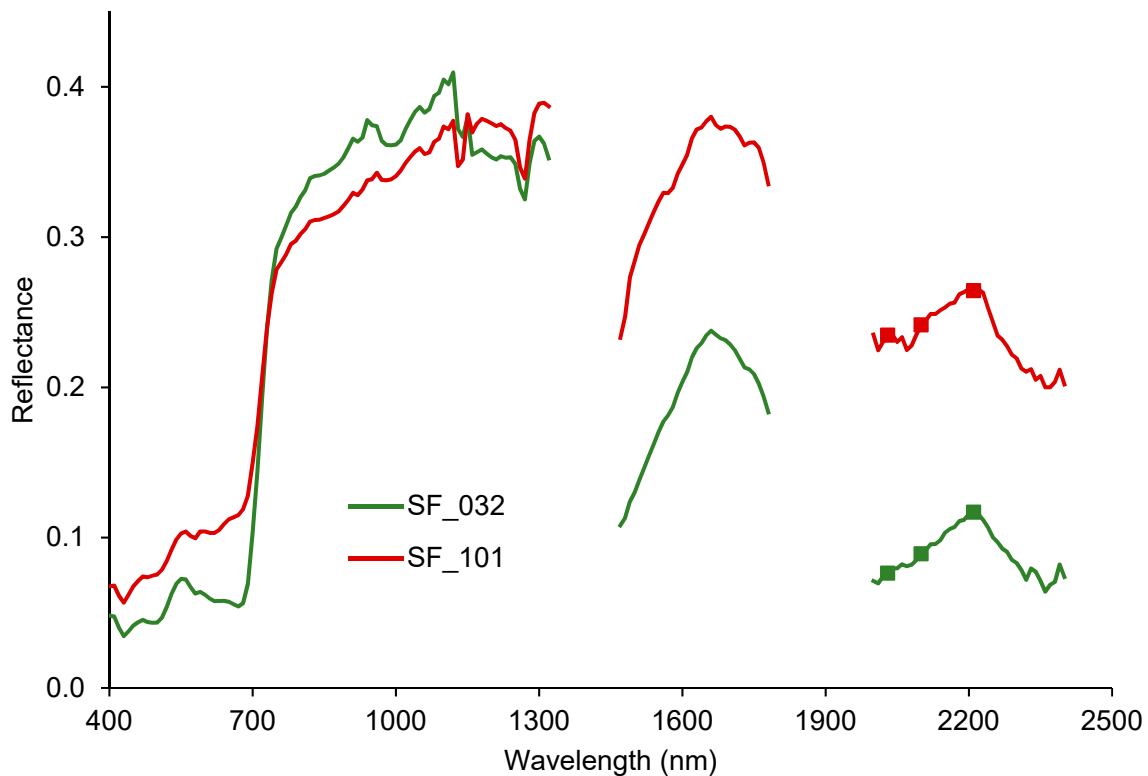
Figure 7. A comparison of a low NPV cover spectrum (SF_032) and moderate NPV cover spectrum (SF_101) with similar CAI values (0.00743 and 0.00795, respectively). Squares indicate the bands used to calculate CAI (see Table 2 for band wavelengths).

PLS and MESMA provided the most accurate estimates of soil fraction. The lack of a diagnostic absorption feature for soil meant that predicted soil fraction was directly or indirectly dependent on predicted GV and NPV fractions, except in the case of PLS. Clay mineral absorption features can reduce CAI values [74], but impacts of mineral absorption features on other methods for estimating fractional cover have not been assessed. Spectroscopic methods that can take into account a variety of soil spectra shapes, like MESMA and PLS, may prove advantageous for estimating fractional cover across diverse soil types. Identifying spectra dominated by minerals present in soil and rock using spectral feature comparison methods, such as USGS Tetracorder [75] and PRISM [63] algorithms, could reduce error by screening for a wide range of mineral spectral signatures.

Although MESMA utilized the full VSWIR spectrum, in some cases it performed more poorly than the other two spectroscopic methods and some narrowband indices. Successful implementation of MESMA depends on endmember selection, and alternative endmember model selection methods could produce lower error in predicted fractions. Techniques for optimal band selection could also lead to improved results from MESMA [76–78]. Machine learning methods like random forests and neural networks could provide alternative methods for utilizing full spectrum data to improve fractional cover estimation [79–81]. In providing our training and validation libraries to the remote sensing community through ECOSIS, we are encouraging others to test alternative methods that may outperform the methods used in this analysis.

Despite its poorer performance, MESMA may still have advantages for global fractional cover mapping. Endmember libraries can be easily expanded to incorporate a diversity of cover types, without requiring retraining like PLS, SFA, or narrowband indices would. Constraints used in MESMA, such as requiring fractions to sum to one, may also be useful for producing outputs with more physically reasonable values. Additionally, MESMA can directly estimate fractional cover from spectra without the additional step of regression to model relationships between metrics and fractional cover.

The training and validation library RMSE values reported in this study (Table 4) are sometimes higher than those described by previous studies. Previous studies typically report RMSE for their model fit to all data rather than for an independent validation dataset, making direct comparison more difficult. Daughtry and Hunt [32] found a 0.141 RMSE for the best-fit linear relationship between CAI and NPV cover. The Daughtry and Hunt [32] spectra were included as part of this study, but our higher RMSE for CAI can be explained by our greater diversity in cover types and use of spatial subsets from the DH-crop dataset for training and validation. Guerschman et al. [20] applied an index-based mixing model to field spectrometer data to obtain RMSE values of 0.104 for GV, 0.121 for NPV, and 0.118 for soil. Guerschman et al. [82] used indices calculated from Landsat and MODIS data to estimate GV, NPV, and soil fractional cover across all of Australia. Their best RMSE values were for three-pixel-by-three-pixel areas from Landsat, producing RMSE values of 0.112 for GV, 0.162 for NPV, and 0.130 for soil. Many factors potentially contribute to differences in RMSE between this study and previous studies, including differences in spectral resolution, differences in methods used to assess fractional cover in the field and from spectra, and the diversity of cover types within a dataset. Use of spatially and temporally partitioned training and validation subsets in this study likely increased error, but hopefully is a closer approximation of errors that could be anticipated from global fractional cover mapping.

This study highlights the urgent need for better and more diverse ground-based estimates of fractional cover. A majority of our field spectra only contained two out of three cover fractions and were not representative of global variability in surface types or fractional cover. Measuring fractional cover is more difficult for higher stature vegetation, but such datasets would greatly improve the diversity of GV cover. Wood and stems are important additions to NPV cover not captured by our library. Even more critical is the inclusion of a greater variety of mineral spectra. Globally, a diversity of mineral signatures can be found in semi-arid and arid regions and areas cleared of vegetation by human activity. For example, in excess of 50 mineral signatures have been identified and mapped in large area coverage of airborne hyperspectral imagery [83,84]. When accounted for, mineral absorption features could increase separability of soil from NPV, leading to more accurate estimates of fractional cover. Due to soil moisture impacts on reflectance spectra, fractional cover accuracy across a range of soil moisture conditions needs to be assessed [33,85]. It is also important to consider that only three cover types and their mixtures were examined in our analysis. GV, NPV, and soil mixtures are common in natural and agricultural ecosystems, but fractional cover of snow [86,87] and impervious surfaces [88,89] are also critically important for some applications. Modification of current techniques or combination of algorithms that allow for multiple cover types and mixtures of cover types may be required for accurate fractional cover mapping at global scales.

Scaling of ground-measured fractional cover to 30 m spatial resolution presents significant challenges. Photography at ground level and transects can capture fine-scale mixtures of GV, NPV, and soil [32], but this type of cover assessment is difficult to scale to coarser spatial resolution. High spatial resolution satellite data can be used to classify fractional cover at meter or sub-meter scales [17], but may miss mixtures in cover that occur at finer spatial scales, like partially senesced grasses and mixtures of green and dead leaves. Imagery from low altitude platforms (i.e., unmanned aerial systems) or field-deployed hyperspectral cameras may offer the best opportunity to capture centimeter-scale mixtures of cover types over areas spanning tens or hundreds of meters. Field assessments of fractional cover need more consistent protocols to account for spatial and temporal variation in cover types and to allow easier integration between datasets collected across a diverse set of ecosystems. An additional future challenge will be quantifying uncertainty in fractional cover estimates. Uncertainty in estimated fractional cover will vary by ecosystem due to variation in vegetation type, vegetation phenology, and the spatial scale and degree of mixing.

5. Conclusions

Our analysis demonstrates that accuracy of fractional cover estimation across GV, NPV, and soil cover types improves when spectroscopic methods are used. PLS, SFA, and MESMA are all promising methods for fractional cover mapping, but for different reasons. PLS produced high accuracies within the validation library, but coefficients were difficult to interpret and portability to other datasets is not clear. Use of PLS for creating fractional cover products from satellite VSWIR data will require more comprehensive training data. SFA performed well for GV and NPV but had higher error for very high fractions of each cover type and provided the lowest accuracy for estimating soil fraction. MESMA trailed PLS and SFA accuracies for GV and NPV cover but could benefit from alternative methods for selecting endmember models and may have greater flexibility for mapping fractional cover of surfaces outside of the GV-NPV-soil triad. The ability of all spectroscopic methods to estimate soil fractional cover remains largely untested due to the relatively small number and low diversity of soil spectra, and variation in soil reflectance will likely prove challenging to any method adopted for global fractional cover mapping. Data from the upcoming PRISMA, HISUI, and EnMAP missions, as well as regional airborne campaigns, will likely assist in capturing this variation and in refining methods for global fractional cover mapping.

References

1. Roberts, D.A.; Smith, M.O.; Adams, J.B. Green vegetation, nonphotosynthetic vegetation, and soils in AVIRIS data. *Remote Sens. Environ.* **1993**, *44*, 255–269. [CrossRef]
2. Chambers, J.Q.; Fisher, J.I.; Zeng, H.; Chapman, E.L.; Baker, D.B.; Hurtt, G.C. Hurricane Katrina's Carbon Footprint on U.S. Gulf Coast Forests. *Science* **2007**, *318*, 1107. [CrossRef] [PubMed]
3. Guerschman, J.P.; Hill, M.J.; Renzullo, L.J.; Barrett, D.J.; Marks, A.S.; Botha, E.J. Estimating fractional cover of photosynthetic vegetation, non-photosynthetic vegetation and bare soil in the Australian tropical savanna region upscaling the EO-1 Hyperion and MODIS sensors. *Remote Sens. Environ.* **2009**, *113*, 928–945. [CrossRef]
4. Meyer, T.; Okin, G.S. Evaluation of spectral unmixing techniques using MODIS in a structurally complex savanna environment for retrieval of green vegetation, nonphotosynthetic vegetation, and soil fractional cover. *Remote Sens. Environ.* **2015**, *161*, 122–130. [CrossRef]
5. Dennison, P.E.; Roberts, D.A. The effects of vegetation phenology on endmember selection and species mapping in southern California chaparral. *Remote Sens. Environ.* **2003**, *87*, 295–309. [CrossRef]
6. Coates, A.R.; Dennison, P.E.; Roberts, D.A.; Roth, K.L. Monitoring the Impacts of Severe Drought on Southern California Chaparral Species using Hyperspectral and Thermal Infrared Imagery. *Remote Sens.* **2015**, *7*, 14276–14291. [CrossRef]
7. Tane, Z.; Roberts, D.; Koltunov, A.; Sweeney, S.; Ramirez, C. A framework for detecting conifer mortality across an ecoregion using high spatial resolution spaceborne imaging spectroscopy. *Remote Sens. Environ.* **2018**, *209*, 195–210. [CrossRef]

8. Roberts, D.A.; Dennison, P.E.; Peterson, S.; Sweeney, S.; Rechel, J. Evaluation of Airborne Visible/Infrared Imaging Spectrometer (AVIRIS) and Moderate Resolution Imaging Spectrometer (MODIS) measures of live fuel moisture and fuel condition in a shrubland ecosystem in southern California. *J. Geophys. Res. Biogeosci.* **2006**. [CrossRef]

9. Elmore, A.J.; Asner, G.P.; Hughes, R.F. Satellite Monitoring of Vegetation Phenology and Fire Fuel Conditions in Hawaiian Drylands. *Earth Interact.* **2005**, *9*, 1–21. [CrossRef]

10. Veraverbeke, S.; Dennison, P.; Gitas, I.; Hulley, G.; Kalashnikova, O.; Katagis, T.; Kuai, L.; Meng, R.; Roberts, D.; Stavros, N. Hyperspectral remote sensing of fire: State-of-the-art and future perspectives. *Remote Sens. Environ.* **2018**, *216*, 105–121. [CrossRef]

11. Riaño, D.; Chuvieco, E.; Ustin, S.; Zomer, R.; Dennison, P.; Roberts, D.; Salas, J. Assessment of vegetation regeneration after fire through multitemporal analysis of AVIRIS images in the Santa Monica Mountains. *Remote Sens. Environ.* **2002**, *79*, 60–71. [CrossRef]

12. Daughtry, C.S.T.; Doraiswamy, P.C.; Hunt, E.R.; Stern, A.J.; McMurtrey, J.E.; Prueger, J.H. Remote sensing of crop residue cover and soil tillage intensity. *Soil Tillage Res.* **2006**, *91*, 101–108. [CrossRef]

13. Daughtry, C.S.T.; Hunt, E.R.; Beeson, P.C.; Milak, S.; Lang, M.W.; Serbin, G.; Alfieri, J.G.; McMarty, G.W.; Sadeghi, A.M. Remote sensing of soil carbon and greenhouse gas dynamics across agricultural landscapes. In *Managing Agricultural Greenhouse Gases: Coordinated Agricultural Research through GRACEnet to Address our Changing Climate*; Liebig, M.A., Franzluebers, A., Follet, R.F., Eds.; Academic Press: Amsterdam, The Netherlands, 2012; pp. 385–408.

14. Numata, I.; Roberts, D.A.; Chadwick, O.A.; Schimel, J.P.; Galvão, L.S.; Soares, J.V. Evaluation of hyperspectral data for pasture estimate in the Brazilian Amazon using field and imaging spectrometers. *Remote Sens. Environ.* **2008**, *112*, 1569–1583. [CrossRef]

15. Davidson, E.A.; Asner, G.P.; Stone, T.A.; Neill, C.; Figueiredo, R.O. Objective indicators of pasture degradation from spectral mixture analysis of Landsat imagery. *J. Geophys. Res. Biogeosci.* **2008**, *113*. [CrossRef]

16. Pullanagari, R.R.; Kereszturi, G.; Yule, I.J. Quantification of dead vegetation fraction in mixed pastures using AisaFENIX imaging spectroscopy data. *Int. J. Appl. Earth Obs. Geoinf.* **2017**, *58*, 26–35. [CrossRef]

17. Asner, G.P.; Heidebrecht, K.B. Spectral unmixing of vegetation, soil and dry carbon cover in arid regions: Comparing multispectral and hyperspectral observations. *Int. J. Remote Sens.* **2002**, *23*, 3939–3958. [CrossRef]

18. Scarth, P.; Roder, A.; Schmidt, M. Tracking Grazing Pressure and Climate Interaction—The Role of Landsat Fractional Cover in Time Series Analysis. In Proceedings of the 15th Australasian Remote Sensing and Photogrammetry Conference, Alice Springs, Australia, 13 September 2010.

19. Nagler, P.L.; Daughtry, C.S.T.; Goward, S.N. Plant Litter and Soil Reflectance. *Remote Sens. Environ.* **2000**, *71*, 207–215. [CrossRef]

20. Guerschman, J.P.; Oyarzabal, M.; Malthus, T.; McVicar, T.R.; Byrne, G.; Randall, L.; Stewart, J. *Evaluation of the MODIS-Based Vegetation Fractional Cover Product*; CSIRO: Canberra, Australia, 2012.

21. Candela, L.; Formaro, R.; Guarini, R.; Loizzo, R.; Longo, F.; Varacalli, G. The PRISMA Mission. In Proceedings of the 2016 IEEE International Geoscience and Remote Sensing Symposium (IGARSS), Beijing, China, 10–15 July 2016; pp. 253–256.

22. Iwasaki, A.; Ohgi, N.; Tanii, J.; Kawashima, T.; Inada, H. Hyperspectral Imager Suite (HISUI)—Japanese hyper-multi spectral radiometer. In Proceedings of the 2011 IEEE International Geoscience and Remote Sensing Symposium, Sendai, Japan, 1–5 August 2011; pp. 1025–1028.

23. Guanter, L.; Kaufmann, H.; Segl, K.; Foerster, S.; Rogass, C.; Chabrillat, S.; Kuester, T.; Hollstein, A.; Rossner, G.; Chlebek, C.; et al. The EnMAP Spaceborne Imaging Spectroscopy Mission for Earth Observation. *Remote Sens.* **2015**, *7*, 8830–8857. [CrossRef]

24. National Research Council. *Earth Science and Applications from Space: National Imperatives for the Next Decade and Beyond*; National Academies Press: Washington, DC, USA, 2007; ISBN 978-0-309-14090-4.

25. Lee, C.M.; Cable, M.L.; Hook, S.J.; Green, R.O.; Ustin, S.L.; Mandl, D.J.; Middleton, E.M. An introduction to the NASA Hyperspectral InfraRed Imager (HyspIRI) mission and preparatory activities. *Remote Sens. Environ.* **2015**, *167*, 6–19. [CrossRef]

26. National Academies of Sciences, Engineering, and Medicine. *Thriving on Our Changing Planet: A Decadal Strategy for Earth Observation from Space*; National Academies Press: Washington, DC, USA, 2018; ISBN 978-0-309-46757-5.

27. Nieke, J.; Rast, M. Towards the Copernicus Hyperspectral Imaging Mission for The Environment (CHIME)—IEEE Conference Publication. Available online: https://ieeexplore.ieee.org/abstract/document/8518384 (accessed on 22 April 2019).

28. Wu, Z.; Snyder, G.; Vadnais, C.; Arora, R.; Babcock, M.; Stensaas, G.; Doucette, P.; Newman, T. User needs for future Landsat missions. *Remote Sens. Environ.* **2019**, *231*, 111214. [CrossRef]

29. Dennison, P.E.; Roberts, D.A.; Chambers, J.Q.; Daughtry, C.S.T.; Guerschman, J.P.; Kokaly, R.F.; Okin, G.S.; Scarth, P.F.; Nagler, P.L.; Jarchow, C.J. *Global Measurement of Non-Photosynthetic Vegetation*; NASA: Washington, DC, USA, 2016; RFI-2 White Paper for the 2017–2027 National Academies Decadal Survey for Earth Science and Applications from Space. Available online: https://hyspiri.jpl.nasa.gov/downloads/RFI2_HyspIRI_related_160517/RFI2_final_DennisonPhilipE.pdf (accessed on 30 August 2019).

30. ASD Inc. *Analytical Spectral Devices, Inc. (ASD) Technical Guide 4th Edition*; ASD Inc.: Alexandria, VA, USA, 1999; p. 136.

31. Kokaly, R.F.; Clark, R.N.; Swayze, G.A.; Livo, K.E.; Hoefen, T.M.; Pearson, N.C.; Wise, R.A.; Benzel, W.M.; Lowers, H.A.; Driscoll, R.L.; et al. *USGS Spectral Library Version 7, Data Series*; U.S. Geological Survey: Reston, VA, USA, 2017.

32. Daughtry, C.S.T.; Hunt, E.R. Mitigating the effects of soil and residue water contents on remotely sensed estimates of crop residue cover. *Remote Sens. Environ.* **2008**, *112*, 1647–1657. [CrossRef]

33. Quemada, M.; Daughtry, C.S.T. Spectral Indices to Improve Crop Residue Cover Estimation under Varying Moisture Conditions. *Remote Sens.* **2016**, *8*, 660. [CrossRef]

34. Roth, K. *Discriminating among Plant Species and Functional Types Using Spectroscopy Data: Evaluating Capabilities Within and Across Ecosystems, across Spatial Scales and through Seasons*; University of California: Santa Barbara, CA, USA, 2014.

35. Roberts, D.; Brown, K.; Green, R.; Ustin, S.; Hinckley, T. Investigating the Relationship Between Liquid Water and Leaf Area in Clonal Populus. In Proceedings of the Summaries of the Seventh JPL Airborne Earth Science Workshop, Pasadena, CA, USA, 12–16 January 1998.

36. Roberts, D.A.; Roth, K.L.; Wetherley, E.B.; Meerdink, S.L.; Perroy, R.L. Hyperspectral Vegetation Indices. In *Hyperspectral Remote Sensing of Vegetation*; CRC Press: Boca Raton, FL, USA, 2019; Volume 2, pp. 3–26.

37. Berk, A.; Anderson, G.P.; Acharya, P.K.; Bernstein, L.S.; Muratov, L.; Lee, J.; Fox, M.; Adler-Golden, S.M.; Chetwynd, J.H.; Hoke, M.L.; et al. MODTRAN 5: A reformulated atmospheric band model with auxiliary species and practical multiple scattering options: Update. International Society for Optics and Photonics. In Proceedings of the Algorithms and Technologies for Multispectral, Hyperspectral, and Ultraspectral Imagery XI, Orlando, FL, USA, 1 April–28 March 2005; Volume 5806, pp. 662–668.

38. Dennison, P.E.; Thorpe, A.K.; Pardyjak, E.R.; Roberts, D.A.; Qi, Y.; Green, R.O.; Bradley, E.S.; Funk, C.C. High spatial resolution mapping of elevated atmospheric carbon dioxide using airborne imaging spectroscopy: Radiative transfer modeling and power plant plume detection. *Remote Sens. Environ.* **2013**, *139*, 116–129. [CrossRef]

39. Thompson, D.R.; Gao, B.-C.; Green, R.O.; Roberts, D.A.; Dennison, P.E.; Lundeen, S.R. Atmospheric correction for global mapping spectroscopy: ATREM advances for the HyspIRI preparatory campaign. *Remote Sens. Environ.* **2015**, *167*, 64–77. [CrossRef]

40. Dennison, P.E.; Daughtry, C.S.T.; Quemada, M.; Roth, K.L.; Numata, I.; Meerdink, S.L.; Wetherley, E.B.; Gader, P.D.; Roberts, D.A. *Fractional Cover Simulated VSWIR Dataset Version 2, Original 10nm spectra*; ECOSIS Spectral Information System: Madison, NA, USA, 2019. [CrossRef]

41. Dennison, P.E.; Daughtry, C.S.T.; Quemada, M.; Roth, K.L.; Numata, I.; Meerdink, S.L.; Wetherley, E.B.; Gader, P.D.; Roberts, D.A. *Fractional Cover Simulated VSWIR Dataset Version 2, Noise & Atmos. Correction Artifacts Included*; ECOSIS Spectral Information System: Madison, NA, USA, 2019. [CrossRef]

42. Ecological Spectral Information System (ECOSIS). Available online: https://ecosis.org/ (accessed on 30 August 2019).

43. Xiao, J.; Moody, A. A comparison of methods for estimating fractional green vegetation cover within a desert-to-upland transition zone in central New Mexico, USA. *Remote Sens. Environ.* **2005**, *98*, 237–250. [CrossRef]

44. Carlson, T.N.; Ripley, D.A. On the relation between NDVI, fractional vegetation cover, and leaf area index. *Remote Sens. Environ.* **1997**, *62*, 241–252. [CrossRef]

45. Rouse, J., Jr.; Haas, R.H.; Schell, J.A.; Deering, D.W. *Monitoring Vegetation Systems in the Great Plains with ERTS*; Third ERTS Symposium, NASA SP-351; NASA: Washington, DC, USA, 1974.

46. Huete, A.; Didan, K.; Miura, T.; Rodriguez, E.P.; Gao, X.; Ferreira, L.G. Overview of the radiometric and biophysical performance of the MODIS vegetation indices. *Remote Sens. Environ.* **2002**, *83*, 195–213. [CrossRef]

47. Hunt, E.R.; Rock, B.N. Detection of changes in leaf water content using Near- and Middle-Infrared reflectances. *Remote Sens. Environ.* **1989**, *30*, 43–54. [CrossRef]

48. Huete, A.R. A soil-adjusted vegetation index (SAVI). *Remote Sens. Environ.* **1988**, *25*, 295–309. [CrossRef]

49. Gamon, J.A.; Field, C.B.; Goulden, M.L.; Griffin, K.L.; Hartley, A.E.; Joel, G.; Penuelas, J.; Valentini, R. Relationships between NDVI, canopy structure, and photosynthesis in three Californian vegetation types. *Ecol. Appl.* **1995**, *5*, 28–41. [CrossRef]

50. Wang, Q.; Adiku, S.; Tenhunen, J.; Granier, A. On the relationship of NDVI with leaf area index in a deciduous forest site. *Remote Sens. Environ.* **2005**, *94*, 244–255. [CrossRef]

51. Daughtry, C.S.T. Discriminating Crop Residues from Soil by Shortwave Infrared Reflectance. *Agron. J.* **2001**, *93*, 125–131. [CrossRef]

52. Nagler, P.L.; Inoue, Y.; Glenn, E.P.; Russ, A.L.; Daughtry, C.S.T. Cellulose absorption index (CAI) to quantify mixed soil-plant litter scenes. *Remote Sens. Environ.* **2003**, *87*, 310–325. [CrossRef]

53. Serbin, G.; Daughtry, C.S.T.; Hunt, E.R., Jr.; Reeves, J.B., III; Brown, D.J. Effects of soil composition and mineralogy on remote sensing of crop residue cover. *Remote Sens. Environ.* **2009**, *113*, 224–238. [CrossRef]

54. Daughtry, C.S.T.; Hunt, E.R.; Doraiswamy, P.C.; McMurtrey, J.E. Remote sensing the spatial distribution of crop residues. *Agron. J.* **2005**, *97*, 864–871. [CrossRef]

55. Serbin, G.; Hunt, E.R., Jr.; Daughtry, C.S.T.; McCarty, G.W.; Doraiswamy, P.C. An improved ASTER index for remote sensing of crop residue. *Remote Sens.* **2009**, *1*, 971–991. [CrossRef]

56. Kokaly, R.F.; Skidmore, A.K. Plant phenolics and absorption features in vegetation reflectance spectra near 1.66 µm. *Int. J. Appl. Earth Obs. Geoinf.* **2015**, *43*, 55–83. [CrossRef]

57. Roberts, D.A.; Gardner, M.; Church, R.; Ustin, S.; Scheer, G.; Green, R.O. Mapping chaparral in the Santa Monica Mountains using multiple endmember spectral mixture models. *Remote Sens. Environ.* **1998**, *65*, 267–279. [CrossRef]

58. Mevik, B.-H.; Wehrens, R. The pls package: Principal component and partial least squares regression in R. *J. Stat. Softw.* **2007**, *18*, 1–23. [CrossRef]

59. Clark, R.N. Spectroscopy of rocks and minerals, and principles of spectroscopy. In *Manual of Remote Sensing*; John Wiley and Sons: New York, NY, USA, 1999; Volume 3, pp. 3–58.

60. Kokaly, R.F.; Clark, R.N. Spectroscopic determination of leaf biochemistry using band-depth analysis of absorption features and stepwise multiple linear regression. *Remote Sens. Environ.* **1999**, *67*, 267–287. [CrossRef]

61. Kokaly, R.F.; Asner, G.P.; Ollinger, S.V.; Martin, M.E.; Wessman, C.A. Characterizing canopy biochemistry from imaging spectroscopy and its application to ecosystem studies. *Remote Sens. Environ.* **2009**, *113*, S78–S91. [CrossRef]

62. Clark, R.N.; Roush, T.L. Reflectance spectroscopy: Quantitative analysis techniques for remote sensing applications. *J. Geophys. Res. Solid Earth* **1984**, *89*, 6329–6340. [CrossRef]

63. Kokaly, R.F. *PRISM: Processing Routines in IDL for Spectroscopic Measurements (Installation Manual and User's Guide, Version 1.0)*; U.S. Geological Survey: Reston, VA, USA, 2011.

64. Roberts, D.A.; Dennison, P.E.; Roth, K.L.; Dudley, K.; Hulley, G. Relationships between dominant plant species, fractional cover and land surface temperature in a Mediterranean ecosystem. *Remote Sens. Environ.* **2015**, *167*, 152–167. [CrossRef]

65. Dennison, P.E.; Roberts, D.A. Endmember selection for multiple endmember spectral mixture analysis using endmember average RMSE. *Remote Sens. Environ.* **2003**, *87*, 123–135. [CrossRef]

66. Dennison, P.E.; Halligan, K.Q.; Roberts, D.A. A comparison of error metrics and constraints for multiple endmember spectral mixture analysis and spectral angle mapper. *Remote Sens. Environ.* **2004**, *93*, 359–367. [CrossRef]

67. Roberts, D.A.; Halligan, K.; Dennison, P.; Dudley, K.; Somers, B.; Crabbe, A. *VIPER Tools User Manual, Version 2.1*; University of California Santa Barbara: Santa Barbara, CA, USA, 2019.

68. Schaaf, A.N.; Dennison, P.E.; Fryer, G.K.; Roth, K.L.; Roberts, D.A. Mapping Plant Functional Types at Multiple Spatial Resolutions Using Imaging Spectrometer Data. *Gisci. Remote Sens.* **2011**, *48*, 324–344. [CrossRef]

69. Roth, K.L.; Dennison, P.E.; Roberts, D.A. Comparing endmember selection techniques for accurate mapping of plant species and land cover using imaging spectrometer data. *Remote Sens. Environ.* **2012**, *127*, 139–152. [CrossRef]

70. Bolster, K.L.; Martin, M.E.; Aber, J.D. Determination of carbon fraction and nitrogen concentration in tree foliage by near infrared reflectances: A comparison of statistical methods. *Can. J. Res.* **1996**, *26*, 590–600. [CrossRef]

71. Qi, Y.; Dennison, P.E.; Jolly, W.M.; Kropp, R.C.; Brewer, S.C. Spectroscopic analysis of seasonal changes in live fuel moisture content and leaf dry mass. *Remote Sens. Environ.* **2014**, *150*, 198–206. [CrossRef]

72. Serbin, S.P.; Singh, A.; McNeil, B.E.; Kingdon, C.C.; Townsend, P.A. Spectroscopic determination of leaf morphological and biochemical traits for northern temperate and boreal tree species. *Ecol. Appl.* **2014**, *24*, 1651–1669. [CrossRef]

73. Singh, A.; Serbin, S.P.; McNeil, B.E.; Kingdon, C.C.; Townsend, P.A. Imaging spectroscopy algorithms for mapping canopy foliar chemical and morphological traits and their uncertainties. *Ecol. Appl.* **2015**, *25*, 2180–2197. [CrossRef] [PubMed]

74. Nagler, P.L.; Marithi Sridar, B.B.; Olsson, A.D.; van Leeuwen, W.J.D.; Glenn, E.P. Hyperspectral remote sensing tools for quantifying plant litter and invasive species in arid ecosystems. In *Hyperspectral Remote Sensing of Vegetation*; Thenkabail, P.S., Lyon, J.G., Huete, A.R., Eds.; CRC Press: Boca Raton, FL, USA, 2018; pp. 97–130, ISBN 978-1-4398-4538-7.

75. Clark, R.N.; Swayze, G.A.; Livo, K.E.; Kokaly, R.F.; Sutley, S.J.; Dalton, J.B.; McDougal, R.R.; Gent, C.A. Imaging spectroscopy: Earth and planetary remote sensing with the USGS Tetracorder and expert systems. *J. Geophys. Res. E: Planets* **2003**, *108*, E12. [CrossRef]

76. Tane, Z.; Roberts, D.; Veraverbeke, S.; Casas, Á.; Ramirez, C.; Ustin, S. Evaluating Endmember and Band Selection Techniques for Multiple Endmember Spectral Mixture Analysis using Post-Fire Imaging Spectroscopy. *Remote Sens.* **2018**, *10*, 389. [CrossRef]

77. Somers, B.; Delalieux, S.; Verstraeten, W.W.; van Aardt, J.A.N.; Albrigo, G.L.; Coppin, P. An automated waveband selection technique for optimized hyperspectral mixture analysis. *Int. J. Remote Sens.* **2010**, *31*, 5549–5568. [CrossRef]

78. Somers, B.; Asner, G.P. Multi-temporal hyperspectral mixture analysis and feature selection for invasive species mapping in rainforests. *Remote Sens. Environ.* **2013**, *136*, 14–27. [CrossRef]

79. Gessner, U.; Machwitz, M.; Conrad, C.; Dech, S. Estimating the fractional cover of growth forms and bare surface in savannas. A multi-resolution approach based on regression tree ensembles. *Remote Sens. Environ.* **2013**, *129*, 90–102. [CrossRef]

80. Jia, K.; Liang, S.; Liu, S.; Li, Y.; Xiao, Z.; Yao, Y.; Jiang, B.; Zhao, X.; Wang, X.; Xu, S.; et al. Global Land Surface Fractional Vegetation Cover Estimation Using General Regression Neural Networks From MODIS Surface Reflectance. *IEEE Trans. Geosci. Remote Sens.* **2015**, *53*, 4787–4796. [CrossRef]

81. Schwieder, M.; Leitão, P.; Suess, S.; Senf, C.; Hostert, P. Estimating fractional shrub cover using simulated EnMAP data: A comparison of three machine learning regression techniques. *Remote Sens.* **2014**, *6*, 3427–3445. [CrossRef]

82. Guerschman, J.P.; Scarth, P.F.; McVicar, T.R.; Renzullo, L.J.; Malthus, T.J.; Stewart, J.B.; Rickards, J.E.; Trevithick, R. Assessing the effects of site heterogeneity and soil properties when unmixing photosynthetic vegetation, non-photosynthetic vegetation and bare soil fractions from Landsat and MODIS data. *Remote Sens. Environ.* **2015**, *161*, 12–26. [CrossRef]

83. Kokaly, R.F.; King, T.V.V.; Hoefen, T.M. *Surface Mineral Maps of Afghanistan Derived from HyMap Imaging Spectrometer Data, Version 2*; US Geological Survey: Reston, VA, USA, 2013.

84. Graham, G.E.; Kokaly, R.F.; Kelley, K.D.; Hoefen, T.M.; Johnson, M.R.; Hubbard, B.E. Application of Imaging Spectroscopy for Mineral Exploration in Alaska: A Study over Porphyry Cu Deposits in the Eastern Alaska Range. *Econ. Geol.* **2018**, *113*, 489–510. [CrossRef]

85. Quemada, M.; Hively, W.D.; Daughtry, C.S.T.; Lamb, B.T.; Shermeyer, J. Improved crop residue cover estimates obtained by coupling spectral indices for residue and moisture. *Remote Sens. Environ.* **2018**, *206*, 33–44. [CrossRef]

86. Salomonson, V.V.; Appel, I. Estimating fractional snow cover from MODIS using the normalized difference snow index. *Remote Sens. Environ.* **2004**, *89*, 351–360. [CrossRef]

87. Rittger, K.; Painter, T.H.; Dozier, J. Assessment of methods for mapping snow cover from MODIS. *Adv. Water Resour.* **2013**, *51*, 367–380. [CrossRef]

88. Powell, R.L.; Roberts, D.A.; Dennison, P.E.; Hess, L.L. Sub-pixel mapping of urban land cover using multiple endmember spectral mixture analysis: Manaus, Brazil. *Remote Sens. Environ.* **2007**, *106*, 253–267. [CrossRef]

89. Ridd, M.K. Exploring a V-I-S (vegetation-impervious surface-soil) model for urban ecosystem analysis through remote sensing: Comparative anatomy for cities. *Int. J. Remote Sens.* **1995**, *16*, 2165–2185. [CrossRef]